JGR Solid Earth

RESEARCH ARTICLE
10.1029/2023JB027952

Key Points:
- We have developed a new joint inversion approach that incorporates stacking of receiver function multiple phases with multiple data sets
- The new approach reduces the trade-offs and improves the determination of deep crustal shear velocity, Moho, and Poisson's ratio
- Application of the new method to the northwestern US produces a more accurate model that exhibits geologically coherent structures

Supporting Information:
Supporting Information may be found in the online version of this article.

Correspondence to:
W. Shen,
weisen.shen@stonybrook.edu

Citation:
Wu, H., Sui, S., & Shen, W. (2024). Incorporating H-*k* stacking with Monte Carlo joint inversion of multiple seismic observables: A case study for the northwestern US. *Journal of Geophysical Research: Solid Earth*, *129*, e2023JB027952. https://doi.org/10.1029/2023JB027952

Received 27 SEP 2023
Accepted 11 JUN 2024

Author Contributions:
Conceptualization: Weisen Shen
Data curation: Hanxiao Wu, Siyuan Sui
Formal analysis: Hanxiao Wu
Funding acquisition: Weisen Shen
Investigation: Hanxiao Wu, Weisen Shen
Methodology: Hanxiao Wu, Weisen Shen
Project administration: Weisen Shen
Resources: Weisen Shen
Software: Hanxiao Wu, Siyuan Sui
Supervision: Weisen Shen
Validation: Hanxiao Wu, Weisen Shen
Visualization: Hanxiao Wu
Writing – original draft: Hanxiao Wu, Weisen Shen

Incorporating H-κ Stacking With Monte Carlo Joint Inversion of Multiple Seismic Observables: A Case Study for the Northwestern US

Hanxiao Wu[1], Siyuan Sui[1,2], and Weisen Shen[1]

[1]Department of Geosciences, Stony Brook University, Stony Brook, NY, USA, [2]Department of Earth Sciences, University of Cambridge, Cambridge, UK

Abstract Accurately determining the seismic structure of the continental deep crust is crucial for understanding its geological evolution and continental dynamics in general. However, traditional tools such as surface waves often face challenges in solving the trade-offs between elastic parameters and discontinuities. In this work, we present a new approach that combines two established inversion techniques, receiver function H-κ stacking and joint inversion of surface wave dispersion and receiver function waveforms, within a Bayesian Monte Carlo (MC) framework to address these challenges. Demonstrated by synthetic tests, the new method greatly reduces trade-offs between critical parameters, such as the deep crustal Vs, Moho depth, and crustal Vp/Vs ratio. This eliminates the need for assumptions regarding crustal Vp/Vs ratios in joint inversion, leading to a more accurate outcome. Furthermore, it improves the precision of the upper mantle velocity structure by reducing its trade-off with Moho depth. Additional notes on the sources of bias in the results are also included. Application of the new approach to USArray stations in the Northwestern US reveals consistency with previous studies and identifies new features. Notably, we find elevated Vp/Vs ratios in the crystalline crust of regions such as coastal Oregon, suggesting potential mafic composition or fluid presence. Shallower Moho depth in the Basin and Range indicates reduced crustal support to the elevation. The uppermost mantle Vs, averaging 5 km below Moho, aligns well with the Pn-derived Moho temperature variations, offering the potential of using Vs as an additional constraint to Moho temperature and crustal thermal properties.

Plain Language Summary Knowing the seismic structure of the deep crust helps us understand Earth's geological history and how continents evolve. However, traditional methods of studying the deep crust face challenges due to tradeoffs that can impact accuracies of the results. In this paper, we present a new approach that combines two existing techniques intending to measure the deep crust more accurately. We tested this method using both synthetic and real data and learned that it works better than previous methods. We applied this method to the Northwestern US and found that the results are aligned with the area's geology, suggesting that the new method is feasible to be applied on a regional scale. The new method provides a more accurate way to study the deep crust and improves the mapping of the uppermost mantle.

1. Introduction

The seismic properties of the deep crust are critical to the understanding of the geological history and dynamic processes of the continents. For instance, the depth from the surface to the lower boundary of the crust, that is, Moho depth, determines the 1st-order variations in surface topography through isostasy (e.g., Schmandt et al., 2015). Seismic velocities of deep crust are often used to infer the magma distributions, or compositional and thermal anomalies (e.g., Hacker et al., 2015; He et al., 2021; Schmandt et al., 2019); Crustal Poisson's ratio, the elastic property related to the ratio between velocities of P and S waves (Vp/Vs), is often associated with the amount of the quartz, a key mineral that dominates the strength and deformation of the lithosphere (Lowry & Pérez-Gussinyé, 2011). As a result, the deep crustal properties such as Moho depth, velocity, and Vp/Vs have been extensively studied using large-scale seismic arrays, for example, USArray (e.g., Ma & Lowry, 2017; Shen & Ritzwoller, 2016; Sui et al., 2022).

Extracting information about the Moho and Vp/Vs ratios is commonly done by analyzing P-wave-converted phases in receiver function (RF) waveforms (e.g., Ammon et al., 1990; Langston, 1977). Zhu and Kanamori (2000) proposed a simple method that employs a grid search in the Moho depth and Vp/Vs space (H-κ) to maximize the stacked amplitude of the P-s phase and the following multiple conversions (i.e., *PpPs* and

Writing – review & editing: Hanxiao Wu, Weisen Shen

PpSs + *PsPs*, Moho-multiples hereafter) in RFs from different events. Thanks to its simplicity, this method quickly gained popularity and has been applied globally, but its dependence on a priori absolute Vs value introduces potential bias in the derived results. On the other hand, surface waves, especially with the development of the ambient noise technique over the past two decades, have proven useful in constraining crustal velocity structure (Ritzwoller et al., 2011) as Rayleigh waves are sensitive to absolute velocity. With the complementary sensitivities of RF and surface waves, the two observables are often combined to infer both absolute velocity and Moho depth (e.g., Juliá et al., 2000; Shen, Ritzwoller, Schulte-Pelkum, et al., 2013). However, the determination of crustal Vp/Vs ratios in such joint inversions using RF waveforms, especially at a continental scale level, is challenging, as: (a) the P-s phase alone cannot solve the trade-off between Moho depth and crustal Vp/Vs; (b) Multiples are often too noisy or complicated to be stacked up (see Section 1 for more details). Consequently, the Moho-multiples are often not used in the joint inversion with RF waveforms (e.g., Shen & Ritzwoller, 2016; Shen, Ritzwoller, & Schulte-Pelkum, 2013), leaving crustal Vp/Vs poorly constrained. Thus, crustal Vp/Vs can only be presumed during the inversion (e.g., Victor et al., 2020; Yang et al., 2020; Zhang & Yao, 2017) except for a few regional studies (e.g., Berg et al., 2021). Additionally, making inaccurate assumptions in crustal Vp/Vs while it trades off with other parameters results in insufficient constraints on all parameters of interest in the continent-scale studies (Shen & Ritzwoller, 2016). An example of not resolving this trade-off for joint inversion will be presented later.

In this study, we propose an innovative approach that combines the widely used H-κ stacking method with the joint inversion of RF waveforms and surface wave dispersion within a Bayesian Monte Carlo (MC) sampling algorithm, aiming to simultaneously resolve the trade-offs mentioned above. Notably, we detailed the challenge we aim to address and the underlying principles behind the methods we proposed to address it in Section 2. Then we outline this new method and demonstrate its feasibility through a comprehensive synthetic test in Section 3. Additionally in Section 4, we apply the new technique to investigate the deep crustal structure in the Northwestern United States (Figure 1), which features diverse geological settings, allowing us to assess the method's effectiveness in characterizing various crustal structures. The area has been investigated intensively in the past decade, providing benchmarks for the results to be compared. In Section 5, we discuss the errors associated with the method and present the new features in the resulting 3-D model. We particularly show how our approach additionally improves the understanding of the uppermost mantle structure. Caveats and potential improvements of the method are also included in this Section. We end the paper with a concise summary.

2. Traditional Approaches and Challenges

2.1. Overview of Surface Waves and Receiver Functions-Related Methods

Surface waves have long been used to infer the subsurface structure of the crust and uppermost mantle (Ekström et al., 1997; Feng et al., 2004; Forsyth & Li, 2005; Levshin et al., 1992; Ritzwoller et al., 2002; Simons et al., 1999; Van Der Lee & Frederiksen, 2005), especially after the development of the ambient noise techniques (e.g., Lin et al., 2009; Yang et al., 2007; Yao et al., 2008). The underlying principle is that the dispersion (i.e., phase and group velocities), the two types of surface wave data used in most traditional inversion, are dominantly sensitive to Vs structure (Lin et al., 2012). While these dispersions are also affected by Vp and density, their generally weaker sensitivity and potential trade-off often prevent Vp and density from being estimated simultaneously with Vs. Additionally, due to the surface waves' sensitivities spanning over broad depth ranges and deepening with periods, they are limited to constraining a smooth Vs model and provide less accurate information about discontinuities such as the Moho. As a result, the receiver function (RF) is often introduced to provide complementary information for Vp/Vs and/or Moho depth.

The RF is a waveform that composites of P-to-S converted phases that reverberate within the subsurface structure beneath the seismometer. Owing to the significant contrast in elasticity and density at Moho, the Moho-converted phases (e.g., *Ps*, *PpPs*, and *PpSs* + *PsPs*) emerge as predominant signals after the direct P wave. For these phases, both their amplitude and arrival times contain important information about the depth and sharpness of the discontinuity, as well as the average crustal Vs and Vp. It is thus preferred to fit the whole RF waveform including these multiples (*PpPs* and *PpSs* + *PsPs*, e.g., Julià et al., 2000) when it is combined with surface waves. Nevertheless, fitting the multiples is challenging. Waveforms from individual earthquakes usually have a low signal-to-noise ratio or are obscured by sedimentary multiples (Yu et al., 2015), hence it requires manual selection of good waveforms and subsequent stacking to enhance the signal. However, the

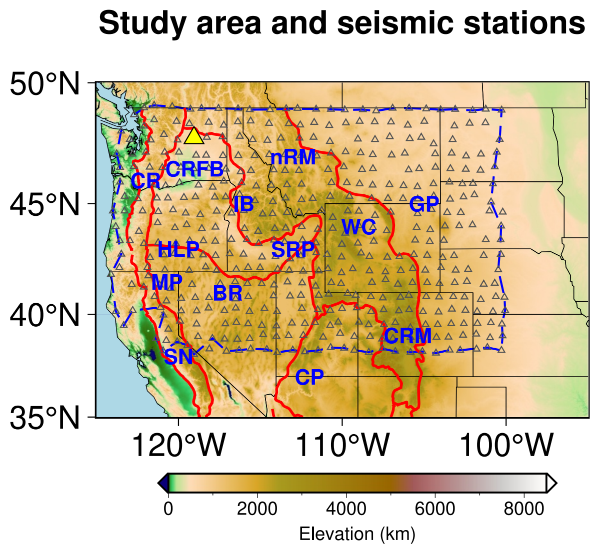

Figure 1. Stations of the EarthScope USArray/Transportable Array (TA) used in this study are shown with triangles. The main physiographic provinces are outlined with red contours (Fenneman & Johnson, 1946). The yellow triangle marks the location of the example station C08A used to demonstrate the new method. The blue dashed line outlines the studied area for which a final 3-D crustal and uppermost mantle model is constructed. Geological and tectonic features are identified with abbreviations: Snake River Plain (SRP), Cascade Range (CR), Columbia River Flood Basalts (CRFB), Idaho Batholith (IB), Basin and Range (BR), High Lava Plains (HLP), Modoc Plateau (MP), Great Plains (GP), Colorado Rocky Mountains (CRM), Colorado Plateau (CP), Wyoming Craton (WC), Sierra Nevada (SN), and northern Rocky Mountains (nRM).

stacking involves complicated corrections to slowness (Chen & Niu, 2013) and/or azimuthal corrections using harmonic stripping (Shen, Ritzwoller, Schulte-Pelkum, et al., 2013), of which the later one may further suppress the multiples. As a result, in many studies employing the popular joint inversion of surface waves and RF waveforms, the stacked RF (referred to as representative RF, hereafter) often focused on the Ps phases, leaving the multiples less emphasized or not used (e.g., Shen & Ritzwoller, 2016; Shen, Ritzwoller, & Schulte-Pelkum, 2013; Shen, Ritzwoller, Schulte-Pelkum, et al., 2013; Yang et al., 2020).

Arrival times of Moho-converted phases in RFs, however, contain rich information on the average velocity and discontinuity depth, which is the basis of the classic H-κ stacking method introduced by Zhu and Kanamori (2000). In this method, the arrival times are calculated based on a simple two-layer, crust-mantle, model, involving only the thickness (i.e., Moho depth) and velocity of the upper layer (i.e., crust), as delineated as follows:

$$T_{Ps} = H \times \left(\sqrt{\frac{1}{V_s^2} - p^2} - \sqrt{\frac{1}{V_p^2} - p^2} \right) \tag{1}$$

$$T_{PpPs} = H \times \left(\sqrt{\frac{1}{V_s^2} - p^2} + \sqrt{\frac{1}{V_p^2} - p^2} \right) \tag{2}$$

$$T_{PpSs+PsPs} = 2H \times \left(\sqrt{\frac{1}{V_s^2} - p^2} \right) \tag{3}$$

$$\kappa = \frac{V_p}{V_s} \tag{4}$$

in which H is the layer thickness, p is the ray parameter, and T_{Ps}, T_{PpPs}, and $T_{PpSs\,+\,PsPs}$ are the arrival times of phase Ps, $PpPs$, and $PpSs + PsPs$, respectively.

For a given (H, κ) pair, the arrival times of different phases can be predicted using equations 1–4 and then the amplitude of individual RFs can be stacked based on the arrival times (referred to as H-κ energy, hereafter):

$$E = \frac{1}{N} \sum_{i=1}^{N} w_1 RF^{[i]}\left(T_{Ps}^{[i]}\right) + w_2 RF^{[i]}\left(T_{PpPs}^{[i]}\right) - w_3 RF^{[i]}\left(T_{PsPs+PpSs}^{[i]}\right). \tag{5}$$

Where i represents the ith event, w_1, w_2, and w_3 represent the corresponding weighting factors applied to each phase, and N is the total event number.

After a grid search in the H-κ model space, the (H, κ) pair that gives the maximized H-κ energy E is considered as the model which fits arrival time best. It is noteworthy that the third equation is dependent on the first two equations, indicating that these three equations facilitate the determination of only two unknown parameters. Thus, an assumption regarding averaged crustal Vs is imperative in the H-κ method. Notably, Yeck et al. (2013) later developed the sequential H-κ stacking method based on this foundation. They separated the sedimentary layer from the crust and assumed a three-layer model (sedimentary layer, crystalline crust layer, and mantle layer) for the stacking. The calculation of arrival times in Yeck et al. (2013) approach involves the thickness and velocity of both the sedimentary and crystalline crust layers. Furthermore, these equations can be adapted to a more refined one-dimensional (1-D) velocity profile (e.g., the model in Figures 2c and 2d):

$$t_{Ps}(m) = \sum_{k=1}^{l} h_k(m) \times \left(\sqrt{\frac{1}{V_{k,s}^2(m)} - p^2} - \sqrt{\frac{1}{V_{k,p}^2(m)} - p^2} \right) \tag{6}$$

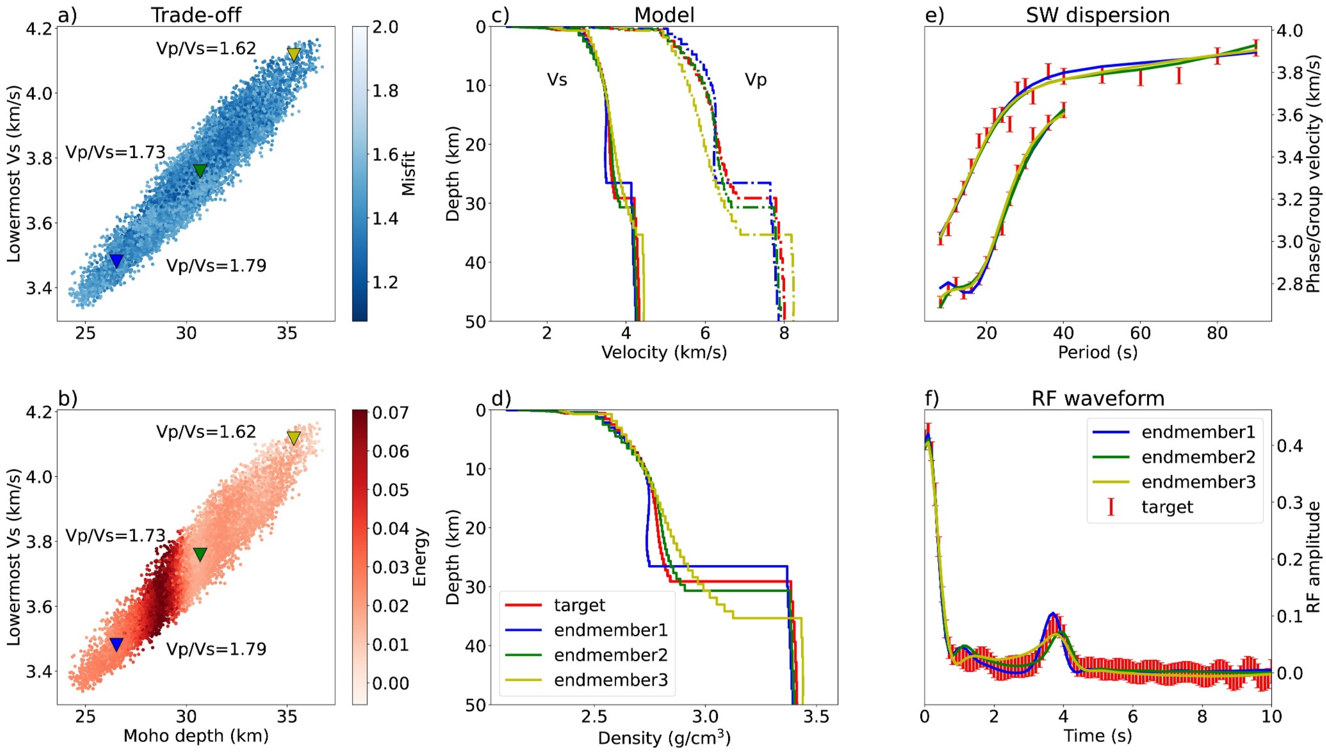

Figure 2. A synthetic example of trade-off. (a) Trade-off between Moho depth and lowermost crust Vs (averaged within 5 km above Moho) observed in a joint inversion of surface wave dispersion and RF waveform. Each blue dot represents a model accepted by the MC joint inversion, color-coded by their joint misfit. The three triangles denote three example models (panel c) used to demonstrate the data fitting in panels (e, f). The corresponding Vp/Vs ratio is labeled next to each example model. (b) Similar to panel a, except that the models are color-coded by their H-κ energy. (c, d) Target model (red) and three example models corresponding to the three triangles in panels (a, b). (e, f) Data fitting of the three example models.

$$t_{PpPs}(m) = \sum_{k=1}^{l} h_k(m) \times \left(\sqrt{\frac{1}{V_{k,s}^2(m)} - p^2} + \sqrt{\frac{1}{V_{k,p}^2(m)} - p^2} \right) \tag{7}$$

$$t_{PsPs+PpSs}(m) = \sum_{k=1}^{l} 2h_k(m) \times \left(\sqrt{\frac{1}{V_{k,s}^2(m)} - p^2} \right) \tag{8}$$

Where l is the number of layers above the Moho, while h_k,$V_{k,s}$, and $V_{k,p}$ denote the thickness, Vs, and Vp of the kth layer, respectively. This generalization allows calculating phase arrivals for a depth-dependent Earth model, usually parameterized and generated by joint inversions (e.g., Shen, Ritzwoller, & Schulte-Pelkum, 2013).

2.2. Challenges and Proposed Solution

As mentioned in the introduction, the insufficiently constrained Vp/Vs highly trades off with other parameters (e.g., Moho depth and Vs), leaving all parameters poorly constrained during a traditional joint inversion of surface wave data and representative RF waveform. An example of this outcome for joint inversion is highlighted in Figure 2, which presents this trade-off based on the result of a synthetic test when crustal Vp/Vs is treated as a free parameter. The scatter plot in Figure 2a shows two crustal parameters, Moho depth and lowermost crustal Vs (defined as the averaged Vs within 5 km above Moho) from the models that can fit the data (joint misfit <1.5). When considering crustal Vp/Vs ranging from 1.6 to 1.9 (typical for crustal rocks), the resulting models exhibit considerable variation in lowermost crustal Vs values, ranging approximately from 3.4 to 4.2 km/s which spans nearly all common lower crustal lithologies (Hacker et al., 2015). They leave the true uncertainties in Moho depth ~ 4–5 km, underscoring the limitations of existing joint inversion methods in effectively constraining these parameters without knowing the accurate crustal Vp/Vs value. Three example models (marked by the triangles in

Figure 2a) are plotted in Figures 2c and 2d together with the target model (red line) for comparison. (For more details, see in Section 3.1), As shown in the plot, the surface wave dispersion and RF waveform predicted based on them are very similar and can fit the data equally well (Figures 2e and 2f), despite being very different in Vs, Vp, and Moho structures.

Adding additional information from H-κ stacking, however, can help distinguish good models from bad ones generated in this synthetic test: for each accepted model, if we not only predict the dispersion and the "representative" RF waveforms but also predict the arrival times of the three Moho converted phases, we could calculate the corresponding stacked energy E according to their arrival times as Equation 5. Then the fitness of arrival time can be evaluated by the H-κ energy E, as color-coded in Figure 2b, while the fitness of surface wave dispersion and representative RF waveform can be evaluated by their misfit. Again, for the three example models in Figure 2, although all of them have reasonable misfits to surface wave dispersion and first 10 s RF waveform, only one subset of them exhibits sufficiently high H-κ energy, indicating a good fit to the arrival times. This demonstrates that if we integrate the H-κ energy into the joint inversion, it is possible to resolve the trade-offs among all three crustal parameters simultaneously.

In this study, we employ a Monte Carlo algorithm in a Bayesian framework to integrate all observables including H-κ stacked energy. Under the Bayesian framework, the result of the inverse problem is presented by the probabilities of the model under (a): prior constraints we impose; (b) the data that is observed. These probabilities are referred to as posterior distributions and can be sampled by a Monte Carlo walk. In our application, the prior constraints represent our basic assumptions in the Earth's model (e.g., monotonically increasing Vs of the crust; positive jump between layers), and the observed data include dispersion curves, representative receiver function waveform, and the individual RF waveforms used to calculate H-κ energy. Further technical details of the method can be found in Section 3, Methods.

3. Methods

In this section, we introduce the workflow of the new method and prove its efficacy through a test using a known target earth model and associated synthetic data sets. As the overall goal is to determine a 1-D seismic structure beneath each station location that effectively fits the seismic data, we first define the model parameterization for the 1-D model, as well as how the synthetic data sets are generated in Section 3.1. Then in Section 3.2, we provide a detailed presentation of the Monte Carlo workflow (Figure 3). Finally, in Section 3.3, the results of the synthetic tests are presented and briefly discussed.

3.1. Model Parameterization and Synthetic Data

The 1-D model employed in this study follows the methodology proposed by Shen et al. (2013b), which characterizes the shallow Earth as comprising three layers: a sedimentary layer, a crystalline crustal layer, and an uppermost mantle layer. Each layer is defined by a depth-dependent Vs profile and is separated by discontinuities at the base of sediment and Moho. The density and Vp profiles are derived from the Vs profiles. For the sedimentary layer, density, and Vp/Vs values are scaled using empirical relationships established by Brocher (2005). The density scaling for the uppermost mantle layer is determined using the empirical relationship introduced by Hacker and Abers (2004), while the Vp/Vs ratio for the uppermost mantle is fixed at a value of 1.789. In contrast to previous joint inversion studies, where the crystalline crustal Vp/Vs was either held constant (e.g., Shen & Ritzwoller, 2016) or scaled from Vs (e.g., Yang et al., 2020), our approach treated it as a free parameter that ranges from 1.55 to 1.95 (see Table S1 in Supporting Information S1 for more information about model parameterization). Furthermore, we impose predetermined rules or boundary conditions to constrain the model space (see Tables S2 and S3 in Supporting Information S1 for more details). Specifically, prior constraints are established to ensure that velocity and density exhibit positive jumps across the discontinuities.

Given this model parameterization, a target model is designed as shown by the red lines in Figure 4a (labeled as "target"), and the proposed approach is applied to the data generated based on this target model. This target model features a monotonically increasing crustal Vp/Vs ratio with a bulk value of ~1.74 ($\frac{V_p}{V_s} = \int_{bottome\ of\ crust}^{top\ of\ crust} \frac{dz}{V_s(z)} / \int_{bottome\ of\ crust}^{top\ of\ crust} \frac{dz}{V_p(z)}$), a crustal thickness of ~29 km, and an average lowermost crustal Vs of ~3.66 km/s. Based on this synthetic model, a synthetic data set is then calculated, including:

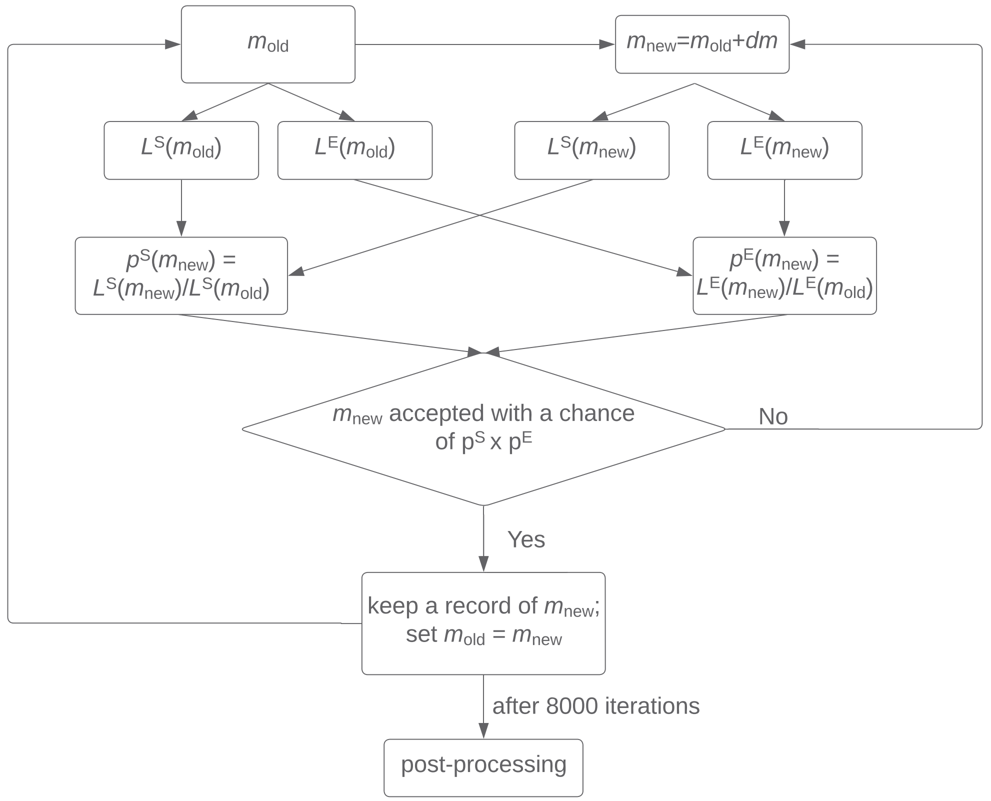

Figure 3. A flowchart of the new joint MC sampling incorporating H-κ stacking. $L^S(m)$ and $L^E(m)$ are likelihood functions associated with the misfit and the H-κ energy, respectively. p^S and $p^E$are the probabilities of being accepted according to misfit-related likelihood and the H-κ energy-related likelihood, respectively. The chance of this model being accepted will be $p^S{*}p^E$. The process highlighted here begins after an initial model is generated, and "post-processing" begins after samplings are performed on 30 different initial models.

1. Individual RF waveforms with different ray parameters (see Figure S1 in Supporting Information S1 for distribution of the ray parameters) for calculating H-κ energy (Figure 4b). The total number of these individual RFs and their ray parameters are set to mimic a real seismic station (R11A of the USArray). These synthetic RFs are calculated based on the synthetic wave from a code developed by Shibutani et al. (1996), which has also been used by Sambridge (1999) and a simple frequency-domain water level deconvolution method.
2. Surface wave dispersion (Figure 4c), including both Rayleigh wave phase and group velocities. These dispersion curves are calculated based on the code developed by Herrmann (2013) using the Thomson–Haskell method with an earth-flattening transformation.
3. A representative RF waveform (Figure 4d) with a ray parameter of 0.06 s/km for which the first 10-s of waveform will be fit.

All data include normally distributed random noise generated based on real practice (see Table S4 in Supporting Information S1 for more information about noise level). When applied to real data, individual RFs will be the raw RF waveforms generated by individual events, and the 3rd data, the first 10-s RF waveform, will be the representative RF that is slowness corrected and azimuthally averaged from all individual RFs from the 1st data (i.e., Shen, Ritzwoller, Schulte-Pelkum, et al., 2013).

3.2. Monte Carlo Sampling

In a Bayesian MC framework, the posterior distribution $\sigma(m)$ is related to the prior distribution $\rho(m)$ through likelihood function L of any given model m:

$$\sigma(m) \propto \rho(m)\,L(m) \tag{9}$$

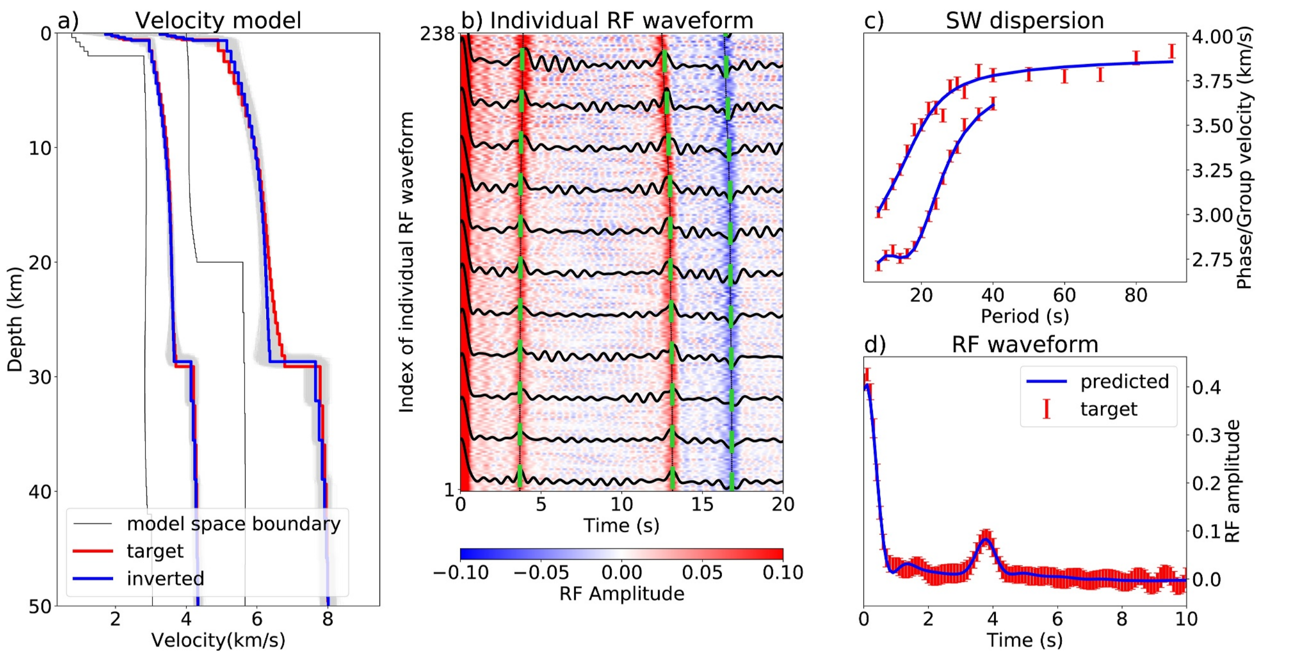

Figure 4. Inversion result of the synthetic test. (a) S-wave and P-wave velocity models. The target model (red lines, the model we used to generate the synthetic data) and the inverted model ensemble (gray profiles) that was accepted by the MC sampling are presented, and the average of the accepted model ensemble is shown by the blue lines, for both P and S wave profiles. The model space for Vs is highlighted by two thin profiles. (b) Data fitting to the H-κ stacked energy. The black lines are examples of RF waveforms with small vertical green bars that denote the predicted arrival time for the Moho-converted phases (e.g., *Ps*, *PpPs*, and *PpSs* + *PsPs* phase) based on the inverted model (blue lines in panel a). All receiver function data involved in the inversion is plotted as colored backgrounds and indexed according to their slowness. (c, d) Data fitting to surface wave dispersion and RF waveform. The red bars represent the synthetic data (generated from the target model) with normally distributed random noise added. The blue lines denote the data predicted by the inverted model (blue lines in panel a).

To sample the posterior distribution, we created the MC chain following the flowchart in Figure 3:

In each chain, a new model (m_{new}) is generated based on the last accepted model (m_{old}) and is accepted or rejected according to a chance p which is determined by comparing its likelihood $L(m_{new})$ to the likelihood of the last accepted model ($L(m_{old})$):

$$p(m_{new}) = \frac{L(m_{new})}{L(m_{old})} \tag{10}$$

For joint inversion of surface wave dispersion and representative RF waveform, likelihood ($L^S(m)$) is defined based on the misfit $S(m)$ between the predicted $d(m)$ and observed data d^{obs}:

$$L^S(m) = \exp(-0.5S(m)) \tag{11}$$

where

$$S(m) = \left(\mathrm{d}(m) - d^{\mathrm{obs}}\right)^T C_e^{-1}\left(d(m)\text{-}d^{\mathrm{obs}}\right) \tag{12}$$

In the new approach, we further defined an additional likelihood function for the H-κ stacked energy for each newly generated model:

$$L^E(m) = \exp(E^n(m))^a \tag{13}$$

Where the E^n represents the normalized stacked energy of predicted *Ps*, *PpPs*, and *PsPs* + *PpSs* phases for all useable tele-seismic events:

10.1029/2023JB027952

$$E^{n}(m) = \frac{1}{N * E^{\mathrm{ref}}} \sum_{\mathrm{i}=1}^{N} w_1 \mathrm{RF}^{[i]}\left(t_{Ps}^{[i]}(m)\right) + w_2 \mathrm{RF}^{[i]}\left(t_{PpPs}^{[i]}(m)\right)\text{-}w_3 \mathrm{RF}^{[\mathrm{i}]}\left(t_{PsPs+PpSs}^{[i]}(m)\right). \tag{14}$$

Where w_k ($k = 1,2,3$) are the weighting of Ps, $PpPs$, and $PsPs + PpSs$ phases and are empirically set to be 0.3, 0.4, and 0.3 in this study, respectively. N is the number of RF waveforms that are stacked. The $E^{ref}$is a reference energy that is used to normalize stacked energy to be mostly between 0 and 1. It can be obtained by performing an initial H-κ stacking algorithm. An ad-hoc factor a is empirically set so that the MC search is guided toward maximizing the H- κ stacked energy at a similar rate of fitting other data. $t_{Ps}(m)$, $t_{PpPs}(m)$, and $t_{PsPs\,+\,PpSs}(m)$ are the arrival times of Ps, $PpPs$, and $PsPs + PpSs$ phases, predicted based on model m, respectively. Although our model is also divided into three basic layers (see Table S1 in Supporting Information S1 model parameterization in Supporting Information S1), each basic layer, in fact, consists of a more refined 1-D velocity profile (as shown in Figure 4a). Therefore, our arrival time is calculated using the adapted Equations 6–8.

As an iterative inversion, MC inversion needs an initial model to begin the iteration. In each round of MC sampling, the initial model is independently randomly generated within the model space. For each inversion, we perform 30 rounds of sampling, with each sampling iterating 8,000 times. This means that one inversion generates 240,000 models (including all accepted and rejected ones). After the whole search (30 rounds of sampling) is complete, we perform several post-processing operations, including:

1. Removing certain models. Near the beginning of the sampling, a few models are accepted before they enter the equilibrium state, so these models should be discarded based on their high misfit to dispersion, receiver function waveforms, and low H-κ stacked energy. Here we adopt the same criteria from Shen et al. (2013b) as the SW + RF misfit threshold (min (joint misfit) + 0.5) and use 0.9*max (H-κ energy) as the energy threshold.
2. Calculate the average of the accepted model ensemble which defines the final inverted model.
3. Calculate the standard deviation of the ensemble.

3.3. Synthetic Test Results

Applying the new workflow to the synthetic data generated based on the target model shown in Figure 2 produces a new posterior ensemble of models, which are shown in Figures 4 and 5. The ensemble average (blue line, labeled as "inverted") of the Vs model, which is considered as the final inverted model, closely resembles the target model, and predicts the arrivals of Moho-converted phases, group and phase velocities, and RF waveforms reasonably well (Figures 4b–4d). Please note that in our target model configuration, the Vp/Vs ratio of the crystalline crust is not a uniform value but varies with depth (Figure S2b in Supporting Information S1). However, during the MC inversion, the Vp/Vs ratio of the crystalline crust is perturbed and inverted as a single value. In other words, this new approach aims to obtain the bulk Vp/Vs ratio of the crystalline crust, instead of a fine 1-D Vp/Vs structure. Consequently, in theory, the Vp structure cannot be accurately resolved (Figure 4a). Using the new approach, the trade-offs between lowermost crust Vs, Moho depth, and crustal Vp/Vs are greatly reduced (Figures 5d–5f), leading to more precise results close to the true values of the target model (Figures 5a–5c). This test demonstrates the feasibility of the proposed approach when applied to synthetic data. However, it is worth noting that the result from the new approach still exhibits considerable uncertainties in crustal Vp/Vs (Figure 5f), mostly due to the remaining trade-off between Vp/Vs and absolute speeds allowed by data uncertainties. To highlight this, we show the data fitting for two endmember models (marked by the triangles in Figure 5f) in the supplemental document (Figure S3 in Supporting Information S1), in which the models with similar Moho but significantly different Vp/Vs fit all data equally well. We also note that a small bias in Moho depth is observed, and this will be discussed in more detail in Section 5.1.

4. Applying the New Method to Northwestern US

To demonstrate the feasibility of our new approach to real data, we applied it to ~450 USArray stations in the northwestern US (Figure 1), where the region has been extensively studied using both H-κ stacking (e.g., Eagar et al., 2011) and surface wave-RF joint inversions (Delph et al., 2018; Shen, Ritzwoller, & Schulte-Pelkum, 2013). The Rayleigh wave dispersion curves and representative RF waveforms with uncertainties are collected from Shen and Ritzwoller (2016), and the individual raw RF waveforms are collected from Sui et al. (2022). The frequency content of individual RFs used for H-κ stacking was chosen by the common choice of

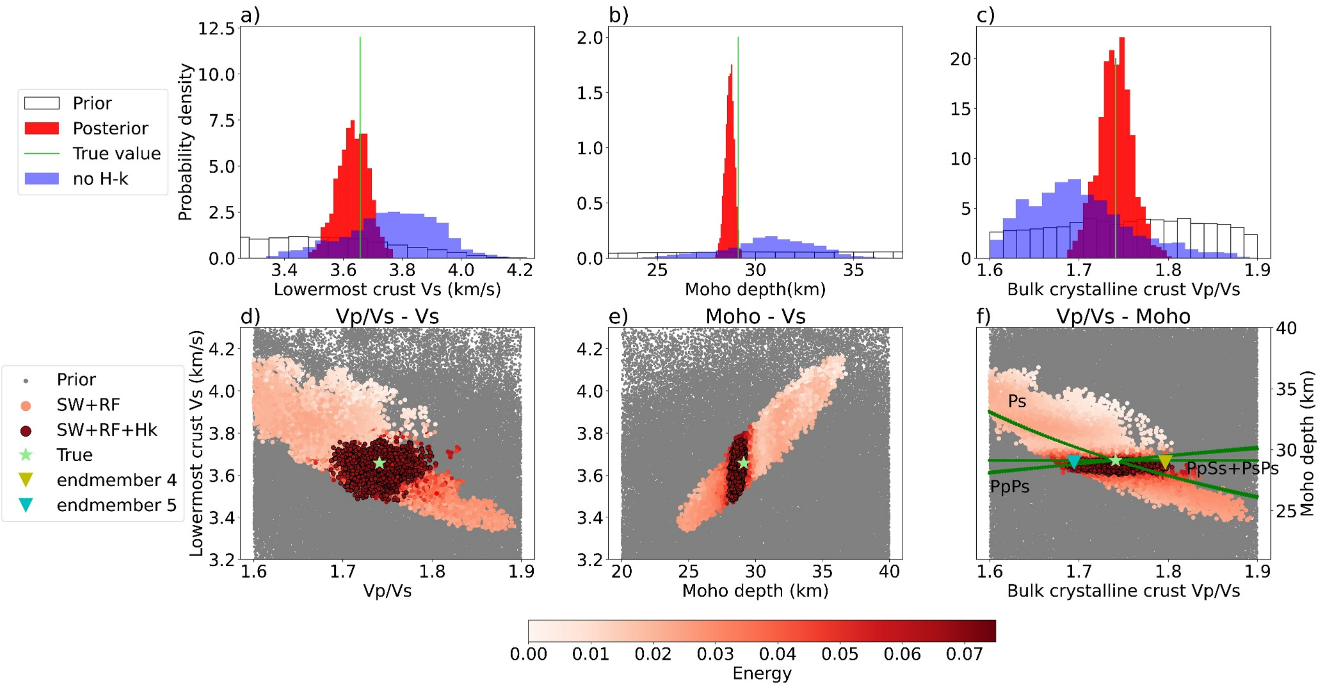

Figure 5. (a–c) Prior and posterior distribution of lowermost crust Vs, Moho depth, and crystalline crust Vp/Vs for the synthetic test of new method. Red histograms represent the posterior distribution generated by the new approach which uses surface wave dispersion, RF waveform, and H-κ stacked energy. Blue histograms represent the posterior distribution generated by traditional joint inversion which only uses SW dispersion and RF waveform. The true value of each parameter is marked by the green vertical lines. (d) Trade-off between the lowermost crust Vs and bulk crystalline crust Vp/Vs. Each reddish dot represents an accepted model, color-coded by its stacked H-κ energy. The results of the traditional joint MC inversion are marked by open dots. The results of the new joint inversion are marked by closed dots. The green stars represent the true values of the target model. (e) Similar to panel d, but for the trade-off between the Moho depth and lowermost crust Vs. (f) Similar to panel d, but for the trade-off between the crystalline crust Vp/Vs and Moho depth. The dark green lines represent the theoretical H-κ relations between Moho depth and bulk crystalline crust Vp/Vs for different Moho-converted phases (Zhu & Kanamori, 2000). The triangles mark two endmember models.

the Gaussian parameter of 2.5 (centered around 1 s). The RFs are computed from three-component seismograms using a time-domain iterative deconvolution method (Ligorría & Ammon, 1999) and then undergo a 5-stage quality control which removes the poor-quality data (Sui et al., 2022).

Figure 6 shows the inversion result of an example station C08A, which is in Almira, WA, north of the Columbia River Flood Basalt. After the rigorous quality control scheme by Sui et al. (2022), this station retained 29 high-quality RF waveforms that can be used to calculate H-κ stacked energy during the MC inversion. As shown in Figure 6b, three major Moho-converted phases can be identified in the individual RF waveforms. The joint MC inversion yielded ~1,800 1-D models, and their average model successfully predicts the arrival times of Moho-converted phases (Figure 6b), while simultaneously fitting the dispersion and the representative RF waveform (Figures 6c and 6d). The posterior marginal distribution (Figures 6e–6g) shows significant reductions in uncertainty compared to the posterior distribution generated by the inversion without H-κ energy: the uncertainty in crustal Vp/Vs is reduced by ~75%; Moho depth uncertainty is reduced by ~90%; and lowermost crust Vs uncertainty is also reduced by ~75%.

Out of the ~450 stations in the study region with all three data types, meaningful results were successfully produced for more than 70% of them, except for those in the Great Plains due to complications arising from the thick sedimentary cover that generates reverberations and masks the Moho-converted phases that we aim to use. Those impacted stations often have higher misfit and low stacked energy and are not used for further analysis. The resulting 1-D models were then combined to form a 3-D seismic model for the crust and uppermost mantle. As this study focuses on how the combination of H-κ stacked energy helps constrain the deep crustal structures (including Moho), the presentation of the results is primarily focused on the corresponding parameters.

As shown in Figure 7, the Vp/Vs map reveals an average Vp/Vs value of ~1.77 for the crystalline crust, with variations highly correlated with tectonic boundaries. High Vp/Vs is found near the High Lava Plain (e.g., S.

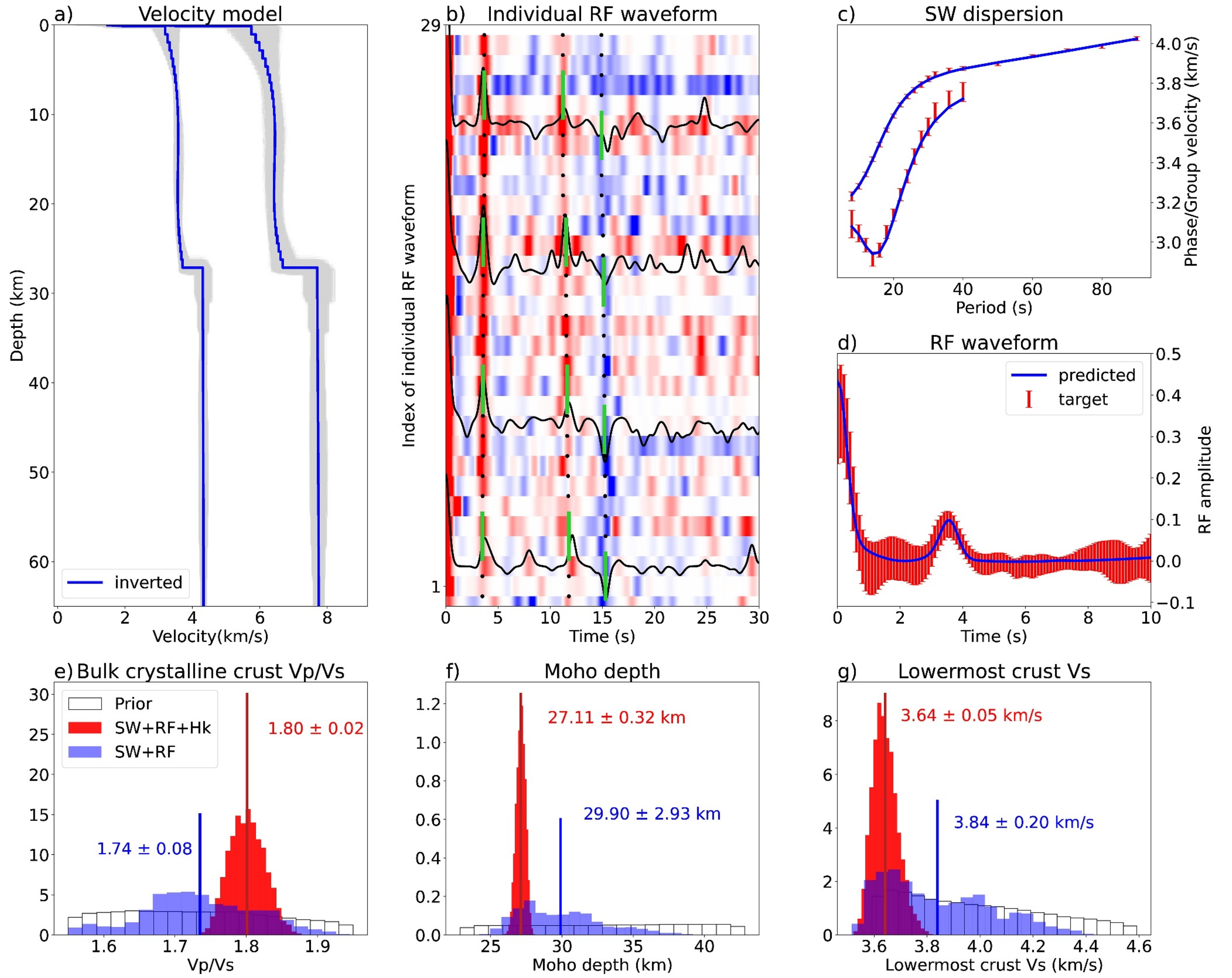

Figure 6. Result for USArray station C08A from the new approach. (a–d) Similar to Figures 4a–4d. (e–g) Similar to Figures 5a–5c. The red and blue vertical lines represent their respective mean, with the specific numerical values (mean ± standard deviation) labeled next to them.

Oregon), which is also connected with relatively high Vp/Vs along the Snake River Plain. The most prominent low Vp/Vs is seen in southern Idaho, northern Oregon, and Washington, encompassing the Idaho Batholith and along the northern Cascades. Both the Moho depth map and lowermost crust Vs map exhibit a west-east dichotomy. The thinnest crust is observed in regions such as the Basin and Range and Columbia River Flood Basalts, while the thicker crust is observed in the Great Plains, Wyoming Craton, and Colorado Rocky Mountains. The western region exhibits lower velocities, except for a relatively higher velocity in the Columbia River Flood Basalt compared to its surroundings.

5. Discussion

5.1. Systematic Errors

Model errors include systematic and nonsystematic errors. The nonsystematic errors should encompass model fluctuations and will be controlled predominantly by errors in the data and trade-offs between model parameters at different depths (Shen & Ritzwoller, 2016). Specifically, our method yields average uncertainties (1-sigma) in crustal thickness of ∼0.5 km (Figure 7d), representing a substantial improvement over previous joint inversion results that did not involve H-κ stacked energy (e.g., Shen, Ritzwoller, & Schulte-Pelkum, 2013), with uncertainties of ∼4 km). This improvement can be attributed to including *PpPs* and *PsPs* + *PpSs* phases in the

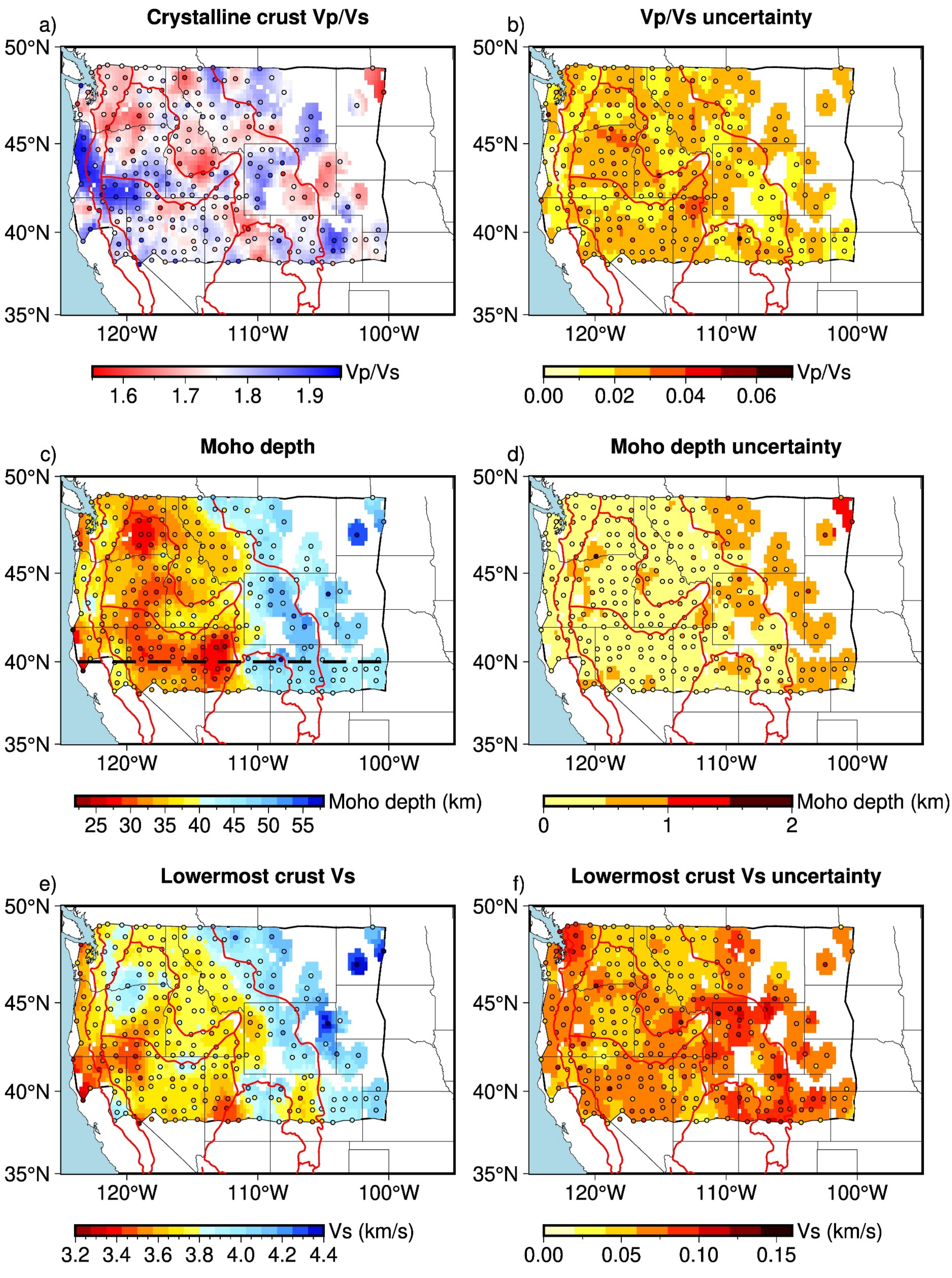

Figure 7. Crustal architecture of the NW US derived from the new approach (a) bulk Vp/Vs of crystalline crust, (c) Moho depth, and (e) lowermost crust Vs (averaged Vs within 5 km above the Moho). (b, d, f) Corresponding 1-standard deviation of the posterior distributions. The dashed black line in panel c corresponds to the Moho depth profile in Figure 8.

inversion process. Furthermore, the more precise determination of Moho depth reduces the uncertainties in the lowermost crustal Vs to ~0.07 km/s, a 30% reduction compared to the uncertainties reported by Shen et al. (2013a) (~0.1 km/s). In this section, we mainly discuss the systematic errors.

Systematic errors come from the assumptions and the method itself. Shen and Ritzwoller (2016) introduced the traditional MC joint inversion method, and they elucidated three pivotal factors linked to systematic errors, which are (a) the scaling of density from Vs; (b) the choice of Q in the mantle; and (c) the scaling relationship between Vp and Vs. Given that our approach is rooted in their method, it inherits these problems to some extent. Regarding the first two factors, Shen and Ritzwoller (2016) conducted an exhaustive discussion, thus obviating the necessity for further elaboration in this context. The third factor is that they were unable to constrain Vp/Vs, and therefore had to set it as a prior parameter. Our novel approach addresses this issue by incorporating H-κ energy into inversion. However, the inclusion of the H-κ data introduces yet another layer of systematic error. The MC inversion involves obtaining a set of models that can reasonably fit the data (i.e., with a misfit below a critical value and H-κ energy above a critical value) and then using their average as the result, instead of selecting the model that fits the data "best" (i.e., smallest misfit or highest energy). This strategy is employed due to the recognition that the presence of errors in the data can lead to an overfitting of the model to these errors when opting for the "best-fitting" model. It is worth noting that as long as the errors in data are completely random and unbiased, this strategy itself should not introduce systematic errors.

In the synthetic test, we also notice a 0.5 km mismatch between the center of the Moho depth posterior distribution and true Moho. These additional biases introduced by the H-κ energy are due to the RF waveform distortion caused by contamination in Moho-converted phases. This bias is more pronounced in case with a sedimentary layer (such as the target model in Section 3.3 synthetic test), where the Moho-converted phases (particularly the $PpPs$ and $PsPs + PpSs$ phases) may be contaminated by additional reverberations generated by other discontinuities (e.g., the bottom of sedimentary layer or/and velocity changes in the lower crust) given that individual phases are limited in frequency. Additional tests show that this contamination to Moho converted phases causes the waveform distortion that either shifts the maximum energy earlier or generates an asymmetric wiggle (see Figures S4–S5, Text S3 in Supporting Information S1 for more details). As the MC search aims to maximize the wave energy, the final inverted model becomes biased, manifesting as a shallower Moho or/and higher Vs (to generate shorter arrival times). It is worth noting that this systematic error primarily manifests in the estimates of Moho depth and Vs, with minimal impact on Vp/Vs—this can be observed in both the posterior distribution (Figures 5a–5c) and the trade-off plots (Figures 5d–5f). This also aligns with the perspective presented in Zhu and Kanamori's paper for H-κ stacking (2000), which suggests that bias in Vs primarily affects the estimation of Moho depth with a lesser impact on Vp/Vs. Finally, additional tests show that (a) the bias introduced by the asymmetrical phases is significantly smaller than the bias introduced by the maximum energy shift; (b) thin sediment is more likely to produce a greater biased Moho depth than a thicker sedimentary model. More details about these additional tests can be found in the supplemental documents (Figures S6 and S7 in Supporting Information S1).

5.2. Improvements and Implications of the New Seismic Model

Seismic attributes are influenced by various factors such as temperature, chemical composition, the presence of partial melting, or fluids. Therefore, conversely, the more accurate seismic models derived from the new method can be used to better infer these factors. Compared with some of the previous studies, our new results demonstrate some improvements and new implications. A detailed benchmark and comparison between our Vp/Vs results and those of previous studies can be found in the supplemental documents, including the results using the traditional H-κ stacking (Figure S8b in Supporting Information S1), sequential H-κ stacking (Figure S8d in Supporting Information S1), and joint inversion of RF and gravity data (Figure S8c in Supporting Information S1). In this section, we mainly discuss the improvements and implications.

One notable feature in the Vp/Vs map is the high Vp/Vs ratios in the crystalline crust of coastal Oregon. The Vp/Vs ratios, ranging from ~1.85 to ~1.95, stand out as particularly high for crustal rocks (Christensen & Mooney, 1995). Several possible mechanisms may produce such elevated Vp/Vs ratios. These include: (a) mafic composition; (b) the existence of the cracks and fractures that lower the Vs; (c) the existence of fluid (e.g., melt) that causes a greater decrease in Vs compared to Vp. It has been speculated that this region might have been accreted to the main continent during the early Eocene and may have a distinct crustal composition compared to other regions (Wells et al., 2014). Additionally, receiver function waveform inversion has identified a layer with

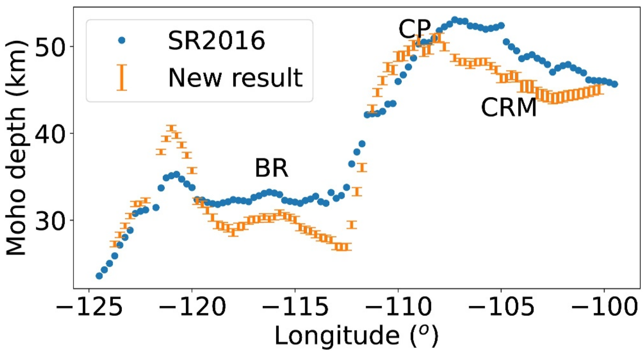

Figure 8. Moho depth profile along the latitude of 40° N, corresponding to the distinct line delineated on Figure 7c. The new results from this study are plotted with error bars. Three key locations are marked by black text: Basin and Range (BR), Colorado Rocky Mountains (CRM), and Colorado Plateau (CP).

slab-bearing fluids at deep crustal depths, potentially representing the subducted oceanic crust (Hansen et al., 2012). Vp/Vs ratios in such a layer are estimated to be as high as ∼2, which can significantly contribute to elevated bulk crustal Vp/Vs measurements as observed in our resulting model.

The new Moho depth result also imparts some new insights. The observation of reduced crustal thickness (compared with SR2016, Figure S9 in Supporting Information S1; Figure 8) beneath the Basin and Range region suggests a diminished contribution of crustal support to the topography through isostasy, indicative of greater dynamic support from the underlying mantle. Additionally, a stronger contrast in crustal thickness between Basin and Range and adjacent tectonic provinces such as Colorado Plateau, as shown in Figure 8, also predicts greater Gravitational Potential Energy (GPE) differences (e.g., Bahadori et al., 2022), which leads to a different GPE-induced stress field.

Another improvement from the new approach is the uppermost mantle Vs. Uppermost mantle Vs can be used to infer the temperature and possible distribution of partial melting (Hansen et al., 2015; Porter & Reid, 2021). However, the depth-velocity trade-off of surface waves often leads to the correlation between uppermost mantle Vs and Moho depth, as demonstrated by the synthetic test (Figure 9a). Due to this significant trade-off, few studies utilize the topmost mantle Vs for mapping the Moho temperature. Instead, much research on mantle temperature focuses on a greater depth, where it is believed that the influence of crustal thickness uncertainties is relatively small (e.g., below 50 km in Rau & Forsyth, 2011). In studies related to Moho temperature, Pn velocity is often utilized (e.g., Boyd, 2020; Schutt et al., 2018). However, with the incorporation of H-κ stacked energy, the accepted model ensemble results in a greatly reduced trade-off between Moho depth and uppermost mantle Vs, and consequently, a better-constrained uppermost mantle Vs (Figure 9a). In this synthetic test, the accepted models obtained through the new approach exhibit a 67% reduction in uppermost mantle Vs uncertainty (0.03 km/s) compared to the case without incorporating H-κ stacked energy (0.09 km/s, Figure 9a). As a result, application of the new method to northwestern US yields an improved uppermost mantle image. As depicted in Figure 9b, the new model exhibits relatively faster Vs beneath the Columbia River Flood Basalt, northern Rocky Mountains, Wyoming Craton, and part of the Basin and Range. Lower Vs in the uppermost mantle is seen near the High Lava Plain, northeast of Basin and Range, the Yellowstone hotspot track, Modoc Plateau, and the Cascadia region. Compared to the SR2016 model (Figure 9c), the new result shows a generally slower uppermost mantle Vs in the northwestern US, except in certain regions such as the northern Cascades, northern Sierra Nevada, southern Modoc Plateau, Wyoming Craton, and the northern margin of the Colorado Plateau.

Given that the trade-off between topmost mantle Vs (averaged Vs within 5 km below Moho) and Moho depth has been reduced, the more accurate Vs has the potential to be used to constrain the Moho temperature, and the usage

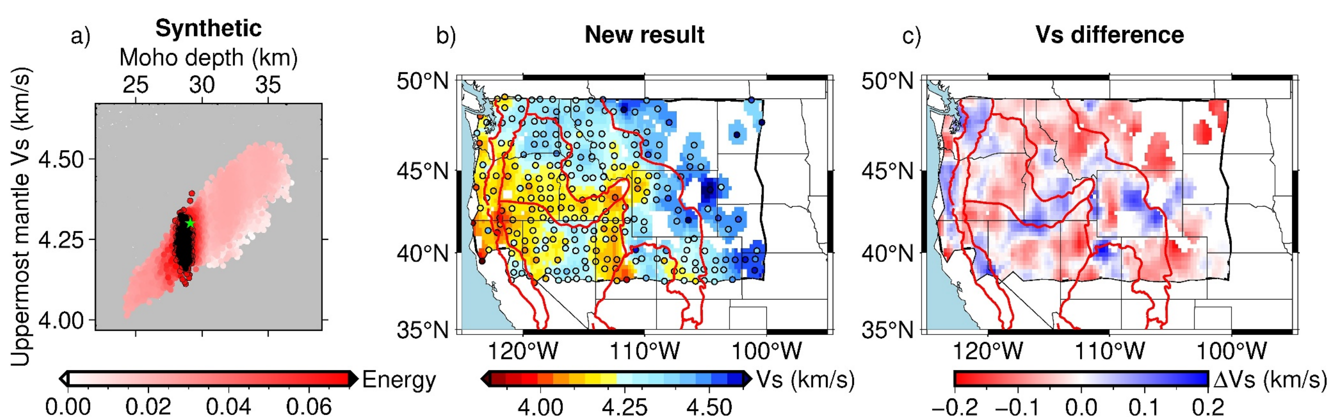

Figure 9. Improvements in uppermost mantle structures of the new model. (a) Trade-off between Moho depth and uppermost mantle Vs (averaged Vs within 5 km below Moho), similar to Figure 2b; (b) Map view of uppermost mantle Vs of our new result; (c) Map view of the differences (new result–SR2016) between our newly obtained uppermost mantle Vs and that of the SR2016 model.

of Vs to constrain uppermost mantle temperature is no longer limited to depths much greater than Moho. In the new map, the overall variation is consistent with the Pn-derived Moho temperature map (Schutt et al., 2018) where the low Vs is found in regions with Moho temperature >800°C (e.g., Yellowstone hotspot track and Cascadia). In some places, discrepancies appear, for example, the Wasatch Fault zone in central-West Utah, where the uppermost mantle Vs is low, but the Pn-derived Moho temperature is not high. However, the low Vs is consistent with the high geothermal heat flux in this area (Blackwell et al., 2011), indicating that the new Vs map provides a useful constraint to refine future Moho temperature models.

5.3. Caveats of the Work and Potential Refinements

The extraction of RFs was performed using the traditional time-domain iterative method, as described in Section 3, without further processing. Also, the following quality control only removes some low-quality data but cannot solve the asymmetric problem caused by the interference of sediment-reverberations. One possible solution is to use higher-frequency RFs to separate the Moho-converted phases and sediment-reverberations since the low-velocity sedimentary layer can result in low-frequency reverberations. A more direct solution is removing the sediment-reverberations from the RFs (e.g., Yu et al., 2015; Z. Zhang & Olugboji, 2023). If these approaches can be applied to the RFs that we used in MC inversion, the asymmetric problem may be solved.

In this work, only the crystalline crust Vp/Vs is set as a free parameter, and the Vp/Vs ratio in the sedimentary layer is simply scaled from the Vs (Brocher, 2005). One possible future improvement of the method is to include the sedimentary-layer phases and reverberations in a sequential H-κ stacking (e.g., Yeck et al., 2013) and include it in the joint MC inversion. Additionally, for the crystalline crust, only the bulk average Vp/Vs is resolved by the data, and it lacks depth sensitivity for investigating the deep crustal structure. The lower crust has been the center of the debate on the composition and evolution of the continental crust in general (e.g., Hacker et al., 2015). To better understand its Vp/Vs ratio, it is thus important to incorporate additional constraints. Lin et al. (2012) and others have made observations of the Rayleigh wave local amplification and show that it provides additional sensitivity to the Vp and density that is different from the phase and group velocities or H/V ratios. If such data can be incorporated in the joint Monte Carlo inversion, additional sensitivity to the particular depth of the crust and possible resolution to the deep crustal structure (e.g., Vp/Vs or density) can be obtained.

5.4. Conclusion

In this paper, we present a novel method that incorporates the traditional H-κ stacking into the MC inversion of surface waves and receiver function waveforms to constrain the architecture of crust and uppermost mantle seismic structure. The feasibility of the new method is demonstrated by synthetic tests and further enhanced by the additional application to the USArray data in NW US. We summarize our findings below:

1. The new approach greatly reduces the trade-offs between lowermost crust Vs, Moho depth, and bulk Vp/Vs ratio of the crystalline crust, eliminating the requirement of assuming crustal Vp/Vs in joint inversions and resulting in more accurate results.
2. In addition to crustal structures, the new approach also enhances the accuracy of upper mantle velocity structure by reducing the trade-off between Moho and upper mantle Vs.
3. Certain reverberations caused by thin sedimentary layers can contaminate the Moho-converted phases by introducing an apparent shift, leading to a mismatch between the maximum energy and the true arrival time. In such cases, the results may introduce bias, primarily affecting the estimation of Vs and Moho depth.
4. When the sedimentary layer is thick enough, some reverberations generated by this sedimentary layer are sufficiently separated from the Moho-converted phases to the extent that there is no energy shift, but the Moho-converted phases are still affected to the point of asymmetry. As a result, there exists a small bias in the obtained result, but much lower than that caused by the apparent maximum energy shift due to sediment contamination.
5. After applying the new method to ~450 USArray stations in NW US, map views of the key crustal parameters (i.e., lowermost crust Vs, Moho depth, and bulk Vp/Vs of crystalline crust) show general consistency with some previous studies but also reveals additional new features.
6. The noticeable high Vp/Vs ratios in the crystalline crust of coastal Oregon suggest the possible presence of mafic composition or the existence of fluid or cracks.

7. The new Moho depth result suggests reduced crustal support in the Basin and Range region, with greater dynamic mantle support and significant GPE differences compared to adjacent tectonic provinces.
8. The uppermost mantle Vs (averaged within 5 km below the Moho) map exhibits good consistency with the Moho temperature map derived from Pn velocity, providing new potential for using Vs to constrain the Moho temperature and crustal thermal properties.

Looking forward, through improved data processing techniques (e.g., removing sediment-related reverberations), the issue of the maximum energy shift present in this new approach may be resolved. Moreover, by incorporating other observables (e.g., local amplification data), the depth resolution for Vp/Vs can be further enhanced, thereby obtaining more accurate deep crustal structures. More accurate seismic structures, in turn, can offer valuable implications in other areas of Earth science. Finally, measurements such as gravity can further serve as a benchmark tool and help reduce the uncertainties in Moho depth and other elastic properties. These potential improvements warrant future investigations after the initial effort summarized in this paper.

Data Availability Statement

The seismic data (including raw data for both surface wave observables and receiver functions) are downloaded from Incorporated Research Institutions for Seismology (IRIS Transportable Array, 2003). The Vp/Vs ratios of EarthScope Automated Receiver Survey are available at (IRIS DMC, 2010). The three key parameters of each station in our study can be found in the supplemental material. The seismic model is scheduled to be available to the public at EarthScope Earth Model Collaborations (EarthScope DMC, 2011) after the manuscript is published.

Acknowledgments

The authors thank William Holt for his valuable discussions. The authors also thank Xiaofei Ma and Anthony R. Lowry for providing the U.S. continental Vp/Vs ratios. The work is mostly supported by NSF OPP-1945856, EAR-2322632. Aspects of the work were also supported by SCEC-21177, EAR-2317868, and OPP-2145410. The facilities of EarthScope Consortium were used for access to waveforms, related metadata, and derived products used in this study. These services are funded through the Seismological Facility for the Advancement of Geoscience (SAGE) Award of the National Science Foundation under Cooperative Support Agreement EAR-1851048. The authors also appreciate two anonymous reviewers, the associate editor of GRL, the associate editor of JGR, and Dr. Vadim Levin who contributed their expertise, time, and invaluable insights to enhance the quality of this paper.

References

Ammon, C. J., Randall, G. E., & Zandt, G. (1990). On the nonuniqueness of receiver function inversions. *Journal of Geophysical Research*, *95*(B10), 15303–15318. https://doi.org/10.1029/jb095ib10p15303

Bahadori, A., Holt, W. E., Austermann, J., Campbell, L., Rasbury, E. T., Davis, D. M., et al. (2022). The role of gravitational body forces in the development of metamorphic core complexes. *Nature Communications*, *13*(1), 5646. https://doi.org/10.1038/s41467-022-33361-2

Berg, E. M., Lin, F.-C., Schulte-Pelkum, V., Allam, A., Qiu, H., & Gkogkas, K. (2021). Shallow crustal shear velocity and Vp/Vs across southern California: Joint inversion of short-period Rayleigh wave ellipticity, phase velocity, and teleseismic receiver functions. *Geophysical Research Letters*, *48*(15), e2021GL092626. https://doi.org/10.1029/2021GL092626

Blackwell, D. D., Richards, M. C., Frone, Z. S., Batir, J. F., Williams, M. A., Ruzo, A. A., & Dingwall, R. K. (2011). SMU geothermal laboratory heat flow map of the conterminous United States.

Boyd, O. S. (2020). Temperature model in support of the U.S. Geological Survey National crustal model for seismic Hazard studies. https://doi.org/10.3133/ofr20191121

Brocher, T. M. (2005). Empirical relations between elastic wavespeed and density in the Earth's crust. *Bulletin of the Seismological Society of America*, *95*(6), 2081–2092. https://doi.org/10.1785/0120050077

Chen, Y., & Niu, F. (2013). Ray-parameter based stacking and enhanced pre-conditioning for stable inversion of receiver function data. *Geophysical Journal International*, *194*(3), 1682–1700. https://doi.org/10.1093/gji/ggt179

Christensen, N. I., & Mooney, W. D. (1995). Seismic velocity structure and composition of the continental crust: A global view. *Journal of Geophysical Research: Solid Earth*, *100*(B6), 9761–9788. https://doi.org/10.1029/95JB00259

Crotwell, H. P., & Owens, T. J. (2005). Automated receiver function processing. *Seismological Research Letters*, *76*(6), 702–709. https://doi.org/10.1785/gssrl.76.6.702

Delph, J. R., Levander, A., & Niu, F. (2018). Fluid controls on the heterogeneous seismic characteristics of the Cascadia margin. *Geophysical Research Letters*, *45*(20), 11021–11029. https://doi.org/10.1029/2018GL079518

Eagar, K. C., Fouch, M. J., James, D. E., & Carlson, R. W. (2011). Crustal structure beneath the High Lava Plains of eastern Oregon and surrounding regions from receiver function analysis. *Journal of Geophysical Research*, *116*(2), B02313. https://doi.org/10.1029/2010JB007795

EarthScope DMC. (2011). Data services products: EMC, A repository of earth models. https://doi.org/10.17611/DP/EMC.1

Ekström, G., Tromp, J., & Larson, E. W. (1997). Measurements and global models of surface wave propagation. *Journal of Geophysical Research*, *102*(B4), 8137–8157. https://doi.org/10.1029/96JB03729

Feng, M., Assumpção, M., & Van der Lee, S. (2004). Group-velocity tomography and lithospheric S-velocity structure of the South American continent. *Physics of the Earth and Planetary Interiors*, *147*(4), 315–331. https://doi.org/10.1016/j.pepi.2004.07.008

Fenneman, N. M., & Johnson, D. W. (1946). Physiographic divisions of the conterminous U.S. *U.S. Geological Survey Data Release*. Retrieved from http://water.usgs.gov/lookup/getspatial

Forsyth, D. W., & Li, A. (2005). Array analysis of two-dimensional variations in surface wave phase velocity and azimuthal anisotropy in the presence of multipathing interference. In A. Levander & G. Nolet (Eds.), *Seismic Earth: Array Analysis of Broadband Seismograms* (pp. 81–97). https://doi.org/10.1029/157GM06

Hacker, B. R., & Abers, G. A. (2004). Subduction Factory 3: An Excel worksheet and macro for calculating the densities, seismic wave speeds, and H_2O contents of minerals and rocks at pressure and temperature. *Geochemistry, Geophysics, Geosystems*, *5*(1). https://doi.org/10.1029/2003GC000614

Hacker, B. R., Kelemen, P. B., & Behn, M. D. (2015). Continental lower crust. *Annual Review of Earth and Planetary Sciences*, *43*(1), 167–205. https://doi.org/10.1146/annurev-earth-050212-124117

Hansen, R. T. J., Bostock, M. G., & Christensen, N. I. (2012). Nature of the low velocity zone in Cascadia from receiver function waveform inversion. *Earth and Planetary Science Letters*, *337*(338), 25–38. https://doi.org/10.1016/j.epsl.2012.05.031

Hansen, S. M., Dueker, K., & Schmandt, B. (2015). Thermal classification of lithospheric discontinuities beneath USArray. *Earth and Planetary Science Letters*, *431*, 36–47. https://doi.org/10.1016/j.epsl.2015.09.009

He, L., Guo, Z., Chen, Y. J., Huang, Q., & Yang, Y. (2021). Seismic imaging of a magma Chamber and melt recharge of the Dormant Datong Volcanoes. *Earth and Space Science*, *8*(12). https://doi.org/10.1029/2021EA001931

Herrmann, R. B. (2013). Computer programs in seismology: An evolving tool for instruction and research. *Seismological Research Letters*, *84*(6), 1081–1088. https://doi.org/10.1785/0220110096

IRIS DMC. (2010). Data services products: EARS EarthScope automated receiver Survey. https://doi.org/10.17611/DP/EARS.1

IRIS Transportable Array. (2003). USArray transportable array [Dataset]. *International Federation of Digital Seismograph Networks*. https://doi.org/10.7914/SN/TA

Juliá, J., Ammon, C. J., Herrmann, R. B., & Correig, A. M. (2000). Joint inversion of receiver function and surface wave dispersion observations. *Geophysical Journal International*, *143*(1), 99–112. https://doi.org/10.1046/j.1365-246x.2000.00217.x

Langston, C. A. (1977). Corvallis, Oregon, crustal and upper mantle receiver structure from teleseismic P and S waves. *Bulletin of the Seismological Society of America*, *67*(3), 713–724. https://doi.org/10.1785/bssa0670030713

Levshin, A., Ratnikova, L., & Berger, J. O. N. (1992). Peculiarities of surface-wave propagation across central Eurasia. *Bulletin of the Seismological Society of America*, *82*(6), 2464–2493. https://doi.org/10.1785/BSSA0820062464

Ligorría, J. P., & Ammon, C. J. (1999). Iterative deconvolution and receiver-function estimation. *Bulletin of the Seismological Society of America*, *89*(5), 1395–1400. https://doi.org/10.1785/bssa0890051395

Lin, F. C., Ritzwoller, M. H., & Snieder, R. (2009). Eikonal tomography: Surface wave tomography by phase front tracking across a regional broad-band seismic array. *Geophysical Journal International*, *177*(3), 1091–1110. https://doi.org/10.1111/j.1365-246X.2009.04105.x

Lin, F. C., Tsai, V. C., & Ritzwoller, M. H. (2012). The local amplification of surface waves: A new observable to constrain elastic velocities, density, and anelastic attenuation. *Journal of Geophysical Research*, *117*(6). https://doi.org/10.1029/2012JB009208

Lowry, A. R., & Pérez-Gussinyé, M. (2011). The role of crustal quartz in controlling Cordilleran deformation. *Nature*, *471*(7338), 353–359. https://doi.org/10.1038/nature09912

Ma, X., & Lowry, A. R. (2017). USArray imaging of continental crust in the conterminous United States. *Tectonics*, *36*(12), 2882–2902. https://doi.org/10.1002/2017TC004540

Porter, R., & Reid, M. (2021). Mapping the thermal lithosphere and melting across the continental US. *Geophysical Research Letters*, *48*(7). https://doi.org/10.1029/2020GL092197

Rau, C. J., & Forsyth, D. W. (2011). Melt in the mantle beneath the amagmatic zone, Southern Nevada. *Geology*, *39*(10), 975–978. https://doi.org/10.1130/G32179.1

Ritzwoller, M. H., Lin, F.-C., & Shen, W. (2011). Ambient noise tomography with a large seismic array. *Comptes Rendus Geoscience*, *343*(8–9), 558–570.

Ritzwoller, M. H., Shapiro, N. M., Barmin, M. P., & Levshin, A. L. (2002). Global surface wave diffraction tomography. *Journal of Geophysical Research*, *107*(B12), ESE 4-1. https://doi.org/10.1029/2002JB001777

Sambridge, M. (1999). Geophysical inversion with a neighbourhood algorithm—I. Searching a parameter space. *Geophysical Journal International*, *138*(2), 479–494. https://doi.org/10.1046/j.1365-246x.1999.00876.x

Schmandt, B., Jiang, C., & Farrell, J. (2019). Seismic perspectives from the western U.S. on magma reservoirs underlying large silicic calderas. *Journal of Volcanology and Geothermal Research*, *384*, 158–178. https://doi.org/10.1016/j.jvolgeores.2019.07.015

Schmandt, B., Lin, F. C., & Karlstrom, K. E. (2015). Distinct crustal isostasy trends east and west of the Rocky Mountain Front. *Geophysical Research Letters*, *42*(23), 10290–10298. https://doi.org/10.1002/2015GL066593

Schutt, D. L., Lowry, A. R., & Buehler, J. S. (2018). Moho temperature and mobility of lower crust in the western United States. *Geology*, *46*(3), 219–222. https://doi.org/10.1130/G39507.1

Shen, W., & Ritzwoller, M. H. (2016). Crustal and uppermost mantle structure beneath the United States. *Journal of Geophysical Research: Solid Earth*, *121*(6), 4306–4342. https://doi.org/10.1002/2016JB012887

Shen, W., Ritzwoller, M. H., & Schulte-Pelkum, V. (2013). A 3-D model of the crust and uppermost mantle beneath the Central and Western US by joint inversion of receiver functions and surface wave dispersion. *Journal of Geophysical Research: Solid Earth*, *118*(1), 262–276. https://doi.org/10.1029/2012JB009602

Shen, W., Ritzwoller, M. H., Schulte-Pelkum, V., & Lin, F. C. (2013). Joint inversion of surface wave dispersion and receiver functions: A Bayesianmonte-Carlo approach. *Geophysical Journal International*, *192*(2), 807–836. https://doi.org/10.1093/gji/ggs050

Shibutani, T., Sambridge, M., & Kennett, B. (1996). Genetic algorithm inversion for receiver functions with application to crust and uppermost mantle structure beneath eastern Australia. *Geophysical Research Letters*, *23*(14), 1829–1832. https://doi.org/10.1029/96GL01671

Simons, F. J., Zielhuis, A., & Van Der Hilst, R. D. (1999). The deep structure of the Australian continent from surface wave tomography. *Lithos*, *48*(1–4), 17–43. https://doi.org/10.1016/S0024-4937(99)00041-9

Sui, S., Shen, W., Mahan, K., & Schulte-Pelkum, V. (2022). Constraining the crustal composition of the continental U.S. using seismic observables. *GSA Bulletin*. https://doi.org/10.1130/b36229.1

Van Der Lee, S., & Frederiksen, A. (2005). Surface wave tomography applied to the north American upper mantle. In *Seismic earth: Array analysis of broadband seismograms* (pp. 67–80). https://doi.org/10.1029/157GM05

Victor, T., Julià, J., White, N. J., & Rodríguez-Tribaldos, V. (2020). Joint inversion of high-frequency receiver functions and surface-wave dispersion: Case study in the Parnaíba basin of Northeast Brazil. *Bulletin of the Seismological Society of America*, *110*(3), 1372–1386. https://doi.org/10.1785/0120190203

Wells, R., Bukry, D., Friedman, R., Pyle, D., Duncan, R., Haeussler, P., & Wooden, J. (2014). Geologic history of Siletzia, a large igneous province in the Oregon and Washington Coast Range: Correlation to the geomagnetic polarity time scale and implications for a long-lived Yellowstone hotspot. *Geosphere*, *10*(4), 692–719. https://doi.org/10.1130/GES01018.1

Yang, Y., Ritzwoller, M. H., Levshin, A. L., & Shapiro, N. M. (2007). Ambient noise Rayleigh wave tomography across Europe. *Geophysical Journal International*, *168*(1), 259–274. https://doi.org/10.1111/j.1365-246X.2006.03203.x

Yang, Y., Yao, H., Wu, H., Zhang, P., & Wang, M. (2020). A new crustal shear-velocity model in Southwest China from joint seismological inversion and its implications for regional crustal dynamics. *Geophysical Journal International*, *220*(2), 1379–1393. https://doi.org/10.1093/gji/ggz514

Yao, H., Beghein, C., & Van Der Hilst, R. D. (2008). Surface wave array tomography in SE Tibet from ambient seismic noise and two-station analysis - II. Crustal and upper-mantle structure. *Geophysical Journal International*, *173*(1), 205–219. https://doi.org/10.1111/j.1365-246X.2007.03696.x

Yeck, W. L., Sheehan, A. F., & Schulte-Pelkum, V. (2013). Sequential h-κ stacking to obtain accurate crustal thicknesses beneath sedimentary basins. *Bulletin of the Seismological Society of America*, *103*(3), 2142–2150. https://doi.org/10.1785/0120120290

Yu, Y., Song, J., Liu, K. H., & Gao, S. S. (2015). Determining crustal structure beneath seismic stations overlying a low-velocity sedimentary layer using receiver functions. *Journal of Geophysical Research: Solid Earth*, *120*(5), 3208–3218. https://doi.org/10.1002/2014JB011610

Zhang, P., & Yao, H. (2017). Stepwise joint inversion of surface wave dispersion, Rayleigh wave ZH ratio, and receiver function data for 1D crustal shear wave velocity structure. *Earthquake Science*, *30*(5–6), 229–238. https://doi.org/10.1007/s11589-017-0197-0

Zhang, Z., & Olugboji, T. (2023). Lithospheric imaging through reverberant layers: Sediments, oceans, and Glaciers. *Journal of Geophysical Research: Solid Earth*, *128*(5), e2022JB026348. https://doi.org/10.1029/2022JB026348

Zhu, L., & Kanamori, H. (2000). Moho depth variation in southern California from teleseismic receiver functions. *Journal of Geophysical Research*, *105*(B2), 2969–2980. https://doi.org/10.1029/1999jb900322